Results in Engineering 30 (2026) 110166

Contents lists available at ScienceDirect

Results in Engineering

journal homepage: www.sciencedirect.com/journal/results-in-engineering

Slate-like alkali-activated roofing tiles produced using copper slag and ground granulated blast furnace slag

Vilma Ducman [a], Wolfgang Wisniewski [a], Afsar Muhammad [b], Davor Kvočka [a], Efthymios Tatsis [b], Lubica Kriskova [b], Yiannis Pontikes [b,*]

[a] *Slovenian National Building and Civil Engineering Institute (ZAG), Dimičeva 12, 1000 Ljubljana, Slovenia*
[b] *Department of Materials Engineering, KU Leuven, Kasteelpark Arenberg 44, 3001 Leuven, Belgium*

ARTICLE INFO

Keywords:
Alkali-activated materials
Durability
Fe rich slag
LCA
Microstructure
Roofing tiles

ABSTRACT

A new type of slate-mimicking roofing tile based on the alkali-activation of an Fe-rich slag has been developed. The main scientific contribution lies in the targeted valorisation of Fe-rich slag for thin, slate-like roofing elements that must satisfy strict roofing-specific requirements, including a limited thickness, low permeability, freeze–thaw resistance, dimensional stability, and high surface quality. Achieving the required properties and optical appearance necessitated a double-layer setup, where a fibre layer primarily provided the required mechanical properties, while a surface layer ensured the desired optical appearance. The microstructure of the produced roofing tiles was analysed using scanning electron microscopy (SEM), energy dispersive X-ray spectroscopy (EDXS) and Hg-porosimetry (MIP), and was compared to reference products on the market. A life cycle assessment (LCA) indicates that the current laboratory-scale production cannot yet compete with established market solutions; however, projected improvements in curing energy efficiency at industrial scale suggest strong potential for environmental competitiveness. Hence these roofing tiles could become an environmentally friendly alternative to current roofing materials. Additionally, a demonstration roof was installed to monitor the long-term performance of the roofing tiles over several years under real seasonal exposure.

1. Introduction

Natural slate has been used as a roofing material since antiquity [1, 2], appreciated for its aesthetic qualities and exceptional durability, which can exceed 100 years [3]. Slate tiles also offer several technical advantages; for example, they exhibit greater resistance to acid rain compared to zinc roofing [4]. Their production is relatively straightforward, provided that suitable deposits and an experienced workforce are available locally. On the contrary, the manufacture of ceramic or concrete tiles requires more advanced technological infrastructure.

Slate stone tiles are typically referred to as “roofing slate”, an umbrella term used for multiple rock types of similar chemical and mineralogical composition, for which a variety of standards have been established [3]. Roofing slate is associated with a comparatively low embodied carbon footprint, reported to range between 0.15 and 1.62 kg CO_2/m^2, substantially lower than that of most alternative roofing materials [3].

While some slate quarries are still operational, many have ceased operations due to resource depletion or a decline in market competitiveness. In fact, slate tiles are currently among the most expensive roofing materials, and their installation requires specialized skills. Concrete tiles provide a lower-cost alternative to clay or slate tiles. They may lack the natural appeal of their counterparts, but they can mimic the look of clay, slate, or shingles. Concrete tiles can outperform clay tiles in colder environments [5], although their intrinsic porosity can be a concern in certain applications. Despite these challenges, slate roofing remains an important part of the regional heritage and architecture of villages and towns throughout Europe [6–8].

One strategy to preserve the traditional slate aesthetic is to develop a sustainable substitute with comparable appearance. Thin, black, cement-based formulations are industrially produced; however, their visual characteristics differ noticeably from natural slate, and the use of cement compromises their sustainability. An alternative approach is the use of alkali-activated materials (AAMs). AAMs—including “geopolymers” when aluminosilicate precursors are employed—are inorganic binders formed through the reaction of solid, typically partially

---

* Corresponding author.
E-mail address: yiannis.pontikes@kuleuven.be (Y. Pontikes).

https://doi.org/10.1016/j.rineng.2026.110166
Received 13 January 2026; Received in revised form 11 March 2026; Accepted 18 March 2026

amorphous precursors with an alkaline activator, most commonly in liquid form. This reaction yields a hardened binder [9], enabling the production of mortar and concrete through the established industrial processing. AAMs have demonstrated potential as substitutes for Portland cement-based products or ceramics, while also offering a means to valorise various industrial by-products. In doing so, they provide environmental benefits to the metallurgical and construction sectors [10] and support circular economy objectives.

The properties of AAMs can be tailored, to some extent at least, to meet the requirements of diverse applications [11]. A major motivation for their development is the substitution of cement-based binders to support decarbonisation targets while reducing the landfilling of industrial by-products [12]. However, conventional AAM precursors such as ground granulated blast furnace slag (GGBFS) and fly ash are becoming scarce, necessitating the identification of alternative sources. Non-ferrous metallurgy (NFM) slags, including those generated during Pb or Cu production, have emerged as promising candidates. Van De Sande et al. [13] conducted a comprehensive investigation of slag chemistry and mineralogy to identify optimal precursors for inorganic polymers, demonstrating that controlled adjustments to melt composition and cooling rates can enhance slag reactivity while simultaneously reducing both cost and environmental impact. In another work, Adediran et al. [14] investigated the development of alkali-activated mortars using Fe-rich fayalitic slag as both the aggregate and the binder, achieving compressive strengths up to 40 MPa for a controlled particle size distribution. There are a number of recent review papers summarising the work on such slags, e.g., Ref. [15].

This work on NFM slags has stimulated broader research on other Fe-rich, pyrometallurgy-derived residues containing amorphous phases [16,17], with encouraging results also reported for blended cements. For instance, Fe–Si–Ca-based residues have been evaluated as unconventional AAM precursors, yielding inorganic polymers with compressive strengths up to 119 MPa [18]. These insights have stimulated work on the vitrification of tailings, trying to mimic pyrometallurgical slags. The recent publication by Giels et al. [19] is a characteristic example.

Primary and secondary copper slags—materials closely related to those examined in the present study—have already been used successfully to produce cast paving tiles with performance comparable to, or exceeding, that of commercial concrete pavers [20]. Similar Fe-rich precursors have also been incorporated into mortars suitable for 3D printing; in one study, formulations containing more than 55 wt% Fe-rich slag achieved compressive strengths of 68 MPa [21] while exhibiting only one-third of the CO_2 footprint of a comparable commercially available cement-based mortar. Still, the research herein is substantially different. For the first time, effort is now placed on fabricating roofing tiles with a textured surface, appearing similar to natural slate tiles. The primary scientific innovation of this study lies in the targeted synergy between Fe-rich copper slag and GGBFS. This combination was selected to exploit the latent hydraulic reactivity of GGBFS together with the alkali-activation potential of the iron–silicate glass present in Fe-rich copper slag. The addition of GGBFS substantially enhances the performance of copper-slag-based inorganic polymers [22, 23].This blend enables the development of high-strength, sustainable binders while successfully valorizing industrial by-products that would otherwise be destined for landfills. Unlike previous research, which has predominantly focused on thicker pavement or façade elements, this work addresses the challenges associated with the development of thin, slate-like roofing tiles. In such thin-profile elements, stringent functional requirements—including impermeability and freeze–thaw resistance—must be met while also mitigating dimensional instability issues such as warpage, which can occur during curing and drying. To address these challenges, the study introduces a double-layer lamination concept specifically engineered to ensure both surface quality and structural integrity in thin-profile applications while reducing the risk of warping. The prepared tiles are composed of a fibre layer, enhancing the mechanical properties [24], covered by a surface layer creating the optical effect. The aesthetics and technical performance were assessed by the relevant standard testing methods, whereas life cycle assessment (LCA) was employed for the sustainability aspects. The microstructure was analysed using scanning electron microscopy (SEM) and mercury intrusion porosimetry (MIP), aiming to provide insights relevant to the tiles' performance.

2. Materials and methods

The two-step casting procedure illustrated in Fig. 1 was employed to manufacture the final tiles for the pilot production: a more liquid surface layer to achieve the desired optical appearance, and a fibre layer of higher viscosity to achieve the required mechanical performance. The surface layer was cast into a mould of 250 × 400 × 5 mm^3, where it set for ca. 3–5 min, while the fibre layer was spread into a matching frame of 250 × 400 × 1 mm^3 using a rolling bar. The frame containing the fibre layer was then flipped onto the mould containing the surface layer and rolled again while being vibrated for 30 s to 1 min max (Knauer Engineering Vibration Table, frequency 50 Hz) to enhance the layer adhesion. The combined layers were subsequently wrapped in plastic to prevent water evaporation (to better control the shrinkage), and cured for 24 h at room temperature (RT) before de-moulding. The de-moulded tiles with a thickness of ca. 6 mm were re-wrapped in plastic, cured for 72 h at 50°C in an oven and unwrapped after cooling to RT and waiting for another 24 h. This curing regime which increases kinetics was selected based on the previous study of Češnovar et al. [25], who reported that the mechanical properties of slags achieved after 3 days of curing at elevated temperature are comparable to those obtained after 28 days under ambient conditions.

Koranel® (Aurubis Beerse) and GGBFS (Ecocem) of the compositions stated in Table 1 were the main precursors used for tile preparation. The chemical compositions were determined using dry-pressed pellets in a WD-XRF Bruker S8 TIGER 4 K spectrometer supported by the Spectraplus software v3.

Further mixture components were disk-milled Koranel®, M800 – quartz sand (Sibelco), "1.7KNSi65", which is potassium silicate with a molar SiO_2/K_2O ratio of 3.3, and a solid content of 35 wt% (Silmaco), mixed with NaOH and water to reach the $SiO_2/(K_2O+Na_2O)$ molar ratio of 1.7 and a water content of 65 wt%, as well as the shrinkage reducing agent (SRA) 2-Methyl-2,4-pentanediol 98% (Alfa Aesar). Polypropylene (PP) fibres (6 mm long, 31–35 μm in diameter, Master Builders) and a black pigment were added to the mixture for the fibre layer. These components were used to prepare mixtures according to Table 2 in 3l Hobart mixers.

The viscosity of the fibre layer mixture was analysed in an MCR 52 rheometer (Anton Paar MCR 52) using a flow sweep test, during which the rotation speed was gradually increased from 0.01 rpm to 100 rpm before decreasing it back to 0.01 rpm. The setting time of the fibre layer mixture was determined using a Vicat EO44N, in which a needle (300 g, 1 mm diameter) is dropped into the paste. Penetration depths were measured at a 5-minute interval.

Samples of both mixtures were prepared using 4 × 4 × 16 cm^3 moulds to measure the flexural and compressive strengths with respective ramp rates of 0.5 mm/min or 2.0 mm/min. The sample dimensions were measured using a Vernier Calliper (Mitutoyo, Neuss, Germany) with a precision of ±0.01 mm. The mechanical properties were measured after reaction times of 7 and 28 days using an Instron 5985 with a 250 kN load cell and a crosshead speed of 2.0 mm/min. Additionally, AAM roof tiles were tested in accordance with the provisions of the standard for roofing products, EN 491 [26]. The flexural strength was determined using the 250 kN load cell and a crosshead speed of 2.0 mm/min (Instron 5985). The water absorption and freeze-thaw resistance were determined in a Kambič climatic chamber executing 25 cooling cycles with a reduction of the air temperature to -20°C within 2 h ± 30 min, a freezing phase where the air temperature is maintained at -20°C for 1 h 15 min ± 15 min and a thawing phase where the samples

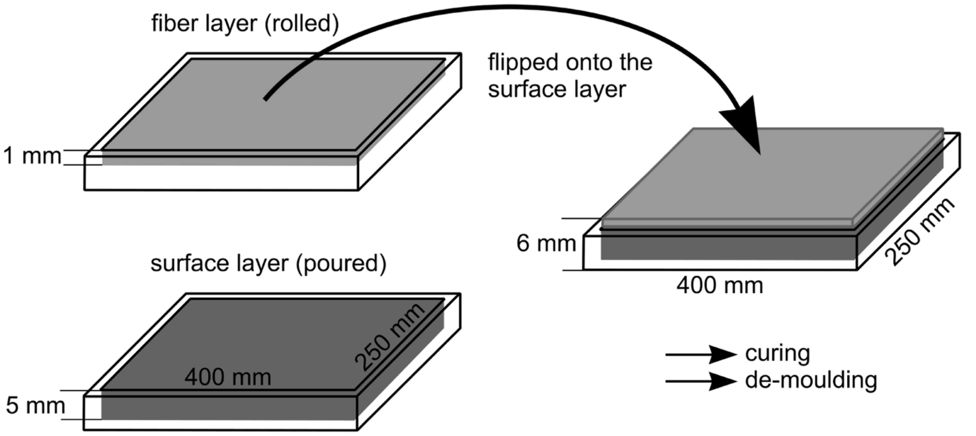

Fig. 1. Schematic illustration of the two-step casting procedure used to manufacture the tiles for pilot production.

Table 1
Precursor compositions in wt% measured using XRF.

Oxide	FeO	SiO_2	Al_2O_3	CaO	ZnO	MgO	P_2O_5	SO_3	others
Koranel®	50.7	24.6	7.6	3.0	6.1	1.2	1.5	-	5.3
GGBFS	-	33.0	11.2	44.8	-	6.8	-	1.7	2.5

Table 2
Mixtures prepared using the respective components.

Components [g]:	Koranel	GGBFS	milled Koranel	M800	1.7KSi 65	2 SRA	PP fibres	pigment
fFibre layer	212.0	37.4	514.0	36.3	112.0	5.3	5.0	-
surface layer	159.0	28.0	386.0	54.5	84.0	4.0	0.0	1.0

are immersed in water with the final temperature of 20°C for 1–2 h. The water permeability was evaluated by sealing the tile into a frame with a silicone sealant and adding a water column of 51 mm to the upper side, which is maintained for 24 h . The bottom side of the tile is monitored for falling water drops, and the tile is considered “impermeable” if no drops fall within 24 h.

The microstructure of sample cross-sections embedded in epoxy resin was analysed using a scanning electron microscope (SEM, JSM-IT500LV, Jeol, Tokyo, Japan). Energy dispersive X-ray spectroscopy (EDXS) was performed using an Ultim Max 65 detector (Oxford Instruments, Abingdon, UK) and the software Aztec 5.0 (Oxford Instruments, Abingdon, UK). The porosity and pore distribution were analysed using a Micromeritics®Autopore IV 9500 (Micromeritics, Norcross, GA, USA).

3. Results and discussion

3.1. Mixture optimization

The main issues to address for the intended tiles are the flow of the prepared mixtures and the porosity and efflorescence of the final product. Initial experiments showed that the most suitable preliminary mixture was too viscous for casting. A first approach to decrease the viscosity by increasing the amount of activating liquid caused warping and would also significantly increase the product costs. Replacing the initially used aggregate river sand with ground Koranel® and decreasing the amount of M800 led to acceptable results without incurring significant costs. Efflorescence was initially addressed by adding silica fume and fly ash to the prepared mixtures, but in the end, the optimizations applied to improve the flow properties also prevented the formation of notable efflorescence.

After 28 days, the surface layer mixtures' compressive strength reached about 100 MPa, whereas their flexural strength reached about 11 MPa. The fibre layer mixture reached a compressive strength > 60 MPa and a flexural strength > 10 MPa after only 7 days.

The stress and viscosity of the fibre layer mixture measured during the flow sweep test were used to measure the yield stress, while the viscosity evolution was used to measure the shear-thinning behaviour. The storage modulus and loss modulus determined based on these measurements are presented in Fig. 2. The storage modulus is dominant and independent from the strain amplitude at a low strain amplitude, indicating the fibre layer mixture to be a viscoelastic gel. The correlating suspension likely contains flocs and is stretched linearly. The critical strain disrupting the suspension network is reached when the storage modulus deviates more than 10% from linearity. It is reached at a strain amplitude of 0.04% in Fig. 2 after which the storage modulus decreases significantly due to network disruption. The flow point refers to the strain amplitude where the loss modulus becomes dominant and is

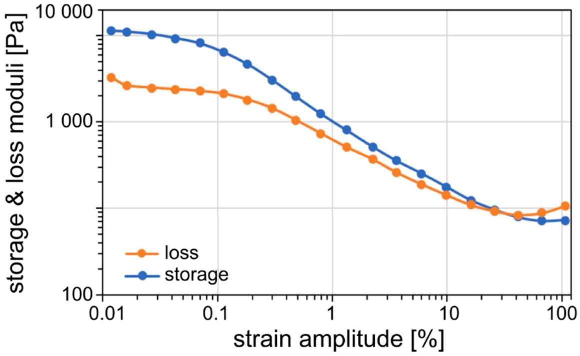

Fig. 2. The evolution in storage and loss modulus of the fibre layer mixture with increasing strain amplitude.

reached at 26% in Fig. 2, i.e., when the mixture begins to flow.

The tested fibre layer mixture exhibited thixotropic behaviour, as its viscosity decreased at 20 rpm and reached equilibrium after 10 s, as shown in Fig. 3. A sudden increase in viscosity was measured when the rotation speed decreased from 20 to 0.5 rpm, indicating that the mixture structure recovers at slow speeds. The recovery was not instantaneous: the equilibrium of a new shear condition, i.e. an almost fully recovered mixture, was approached during the period from 60 to ca. 90 s, i.e. over a time of ca. 30 s.

Fig. 4 illustrates that the fibre layer mixture showed shear-thinning, i.e., a high viscosity up to 31,367 Pa•s at low rotation speeds but a low viscosity down to 171 Pa•s. This is related to flocculation/colloidal breakdown of colloidal particles, as well as the breaking of early bonds formed amongst them. The trend towards plateaus at high rotation speeds indicates all flocs/structure in the mixture was broken, and a Newtonian behaviour was almost reached. The hysteresis loop presented in Fig. 4 is closed, indicating that the viscosity rapidly adapted to the new shear conditions. The fibre layer mixture exhibited a yield stress of 370 Pa when a rotational speed of about 0.25 rpm was reached, after which the stress increased with increasing rotational speed as is discernible in Fig. 4, due to the friction between the particles in the mixture. Due to shear thinning behaviour, the mixture flows easily, and fibres and aggregates become aligned while defects are removed. This results in better internal cohesion and the removal of air pockets, leading to increased strength. The thixotropic behaviour helps lock the internal structure once the external load (via vibration or rolling pin) is stopped, so the alignment of the fibres is maintained. This thixotropic behaviour also helps retain water and prevents its migration to the top surface, which would otherwise create pores that can act as crack initiation sites.

The Vicat test of the fibre layer mixture showed that setting starts about 30 min after pouring, where a penetration depth of ca. 41 mm was measured. It reached 0 after about 45 min, meaning the mixture was fully set at this time, and the working time is rather short. This can be an advantage as these tiles can be safely demoulded 1 h after casting as a sufficient early strength is reached.

3.2. Pilot production of AAM roof tiles

Fig. 5 a) compares the visual appearance of tiles from an initial trial to the final trials. The mixtures of the initial trials and samples produced using only the fibre layer mixture showed a significant porosity discernible in Fig. 5 b) which is undesirable for roofing tiles because it usually decreases the frost resistance. On the other hand, such pores can attract plants and mosses to create green roofs, e.g., in warm climates where freezing is not a relevant issue. Treating samples cast into glass moulds by vibration to remove air bubbles before curing them for 24 h at 50°C led to comparably undesirable results. Switching the mould material to polyurethane and coating it with silicone oil before casting the mortar led to a sufficiently low porosity of the roofing tiles of the final production, visualized in Fig. 5 b).

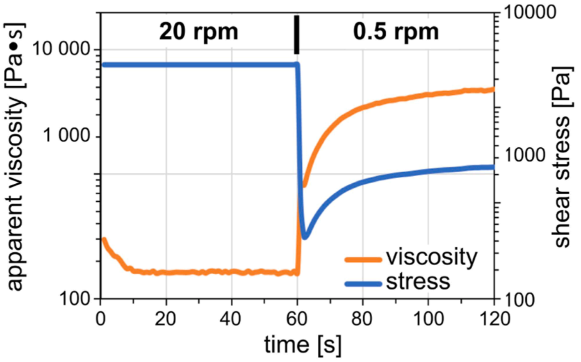

Fig. 3. Viscosity and stress measured at shear rates of 20 rpm or 0.5 rpm in the fibre layer mixture, each for 1 min.

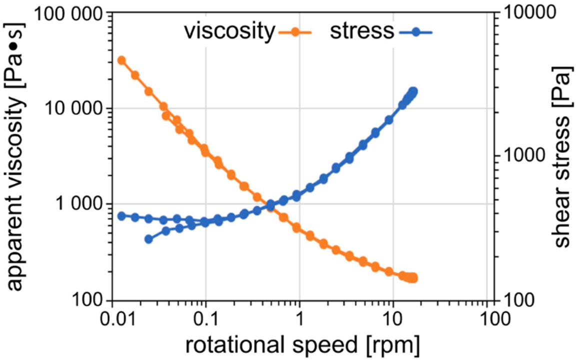

Fig. 4. The evolution in stress and viscosity with increasing and decreasing rotational speed.

Upon completing and optimizing the trial stage at the lab scale with a satisfactory reproducibility, the process was upscaled to a pilot production. The mobile upscaling unit at SREMat featured in Fig. 6 a) was used to produce AAM roofing tiles at larger scale and provide the proof of concept. Fig. 6 b) presents a fibre layer produced at this line, whereas Fig. 6 c) shows the surface layer being rolled onto the fibre layer. Upscaling is important because it can reveal potential barriers in AAM technology applications [27,28]. These include technical parameters, such as rheological properties in the fresh state, but also cracks caused by high shrinkage or insufficient drying/curing [29–31]. Special attention should be paid to occupational safety as highly alkaline solutions are used in the alkali activation of these materials.

3.3. Testing the AAM roofing tiles

A plan for testing relevant properties was based on surveying the standards for roofing products EN 491 [26]. Results of the mechanical resistance, water impermeability, water absorption, and freeze-thaw resistance were also compared to selected commercially available products.

Selected performance parameters of competitive products, i.e., tiles made of slate stone or concrete, were determined and compared to the AAM roofing tiles. The maximum load during a transverse strength test, respectively, reached 677 N, 185 N, or 143 N before 25 cycles of freezing and thawing and 495 N, 197 N, or 89 N after it, meaning the AAM roofing tiles show a lower transverse strength than the compared products. A reduction in strength due to freezing is often observed when water in the pores freezes and expands, causing cracking [5,8]. Although the investigated tiles did not show a visible degradation comparable to slate stone, internal degradation still occurred, as shown by the mechanical strength decrease after freezing, discernible in Table 3. Conversely, a slight increase in the strength of concrete tiles observed after 25 freeze–thaw cycles may be attributed to an ongoing late hydration and/or carbonation processes. Long term carbonation could also lead to pore refinement and a partial densification of the microstructure in AAM tiles which may enhance the mechanical performance [32–34] which will be tested after several years of exposure.

Testing the water permeability showed that the permeability coefficient was always 0, and water drops failed to form on the underside of all tiles, both before and after 25 cycles of freezing and thawing. Sample damage was only observed in the form of delamination for one stone tile (out of six) but not for slate tiles during the test series.

The porosity in the final AAM roofing tiles was analysed using MIP, and the results are compared to commercially available products in Fig. 7; selected values are presented in Table 4. The lowest porosity of 4.04 % was measured for the concrete tiles which do not contain gel pores according to Fig. 7, whereas larger pores from ca. 9 to over 100 μm

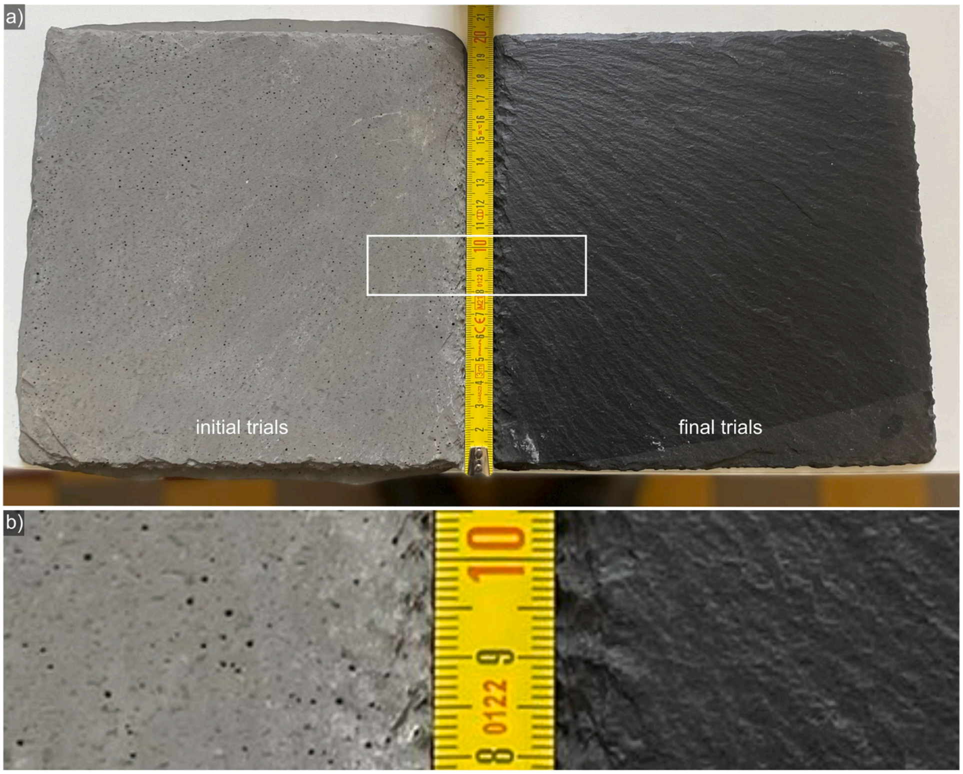

Fig. 5. Digital photographs a) comparing the too porous AAM tiles of the initial trials with the sufficiently porous AAM tiles of the final production. The framed area is presented in greater detail in b) to visualize the pore size and surface texture.

Fig. 6. Upscaling the pilot production: a) Production line used at SREMat KU Leuven, b) complete fibre layer and c) rolling on the cover layer in the mould.

Table 3
Properties of products from pilot production compared to the reference commercial products.

Test method		AAM tiles	concrete	stone
mechanical resistance	max. load transverse strength (production) [N]	143 (±24)	185 (±11)	699 (±197)
	max. load transverse strength (25 freeze-thaw cycles) [N]	89 (±34)	197 (±26)	495 (±181)
water impermeability	water drops on the tile underside [yes/no]	no	no	no
	impermeability coefficient (production) [/]:	0	0	0
	impermeability coefficient (25 freeze-thaw cycles) [/]:	0	0	0
freeze-thaw resistance	occurrence of damage [yes/no]	no	no	stratification of sample no. 6

were also present. The slate stone and AAM tiles exhibited a higher porosity and larger pore size than concrete tiles throughout most of the measured range. Both contained gel pores; most of the pores in the AAM tile have diameters below 0.01 μm, which is typical for AAM [35–38]. The porosity is crucial concerning the freeze- thaw resistance where the pore structure combined with the gel type play a significant role in the degradation mechanism. A stable N-A-S-H gel network typically maintains its mechanical properties during freezing despite considerable pore expansion. In contrast, C-A-S-H gel networks in partially Ca-activated alkali-activated cementitious materials are susceptible to stronger freeze-thaw deterioration [39]. Besides the gel type, many other factors influence the freeze-thaw resistance of concrete or alkali-activated materials. For example, insufficient hydration at early ages results in a porous and discontinuous microstructure, which

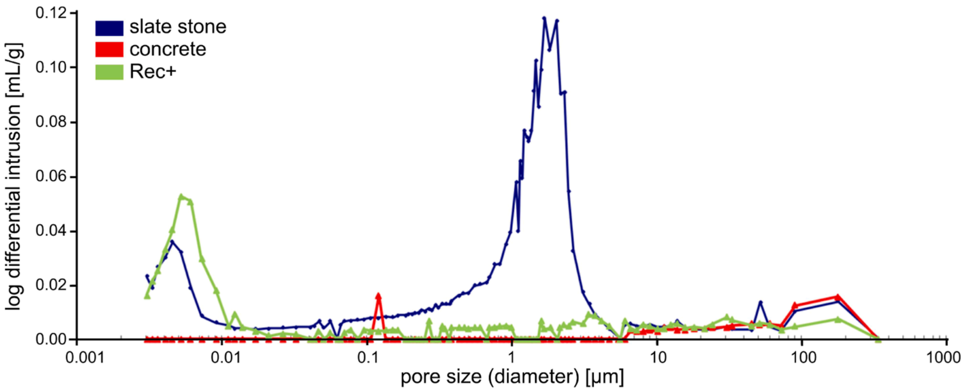

Fig. 7. Pore size distribution measured for AAM roofing tiles and commercially available roofing tiles.

Table 4
Parameters related to the porosity obtained by MIP.

Property	AAM tiles	concrete	stone
porosity [%]	10.92	16.12	4.04
density [g/cm^3]	2.78	1.92	2.69
average pore size [µm]	0.01	0.03	1.98
median pore size -based on calculation from surface [µm]	0.01	0.01	0.14
median pore size -based on calculation from volume [µm]	0.02	1.48	103.16

significantly reduces frost resistance because ice formation in capillaries and larger pores generates internal stresses that exceed the tensile capacity of the immature matrix [40]. Freeze-thaw resistance depends not only on mixture parameters and curing conditions, but also to a great extent on the pore size distribution and the volume of different pore types within the hardened cement, which are consequences of the first two factors. Studies have shown that a higher proportion of finer pores, particularly innocuous gel pores (approximately 1–10 nm), contributes little to frost damage because they do not fill with water and thus do not generate significant freezing pressures, while larger capillaries and mesopores (on the order of tens to hundreds of nanometers) are most critical for freeze-thaw deterioration due to water ingress and ice expansion [41].

The microstructure of the produced AAM roofing tiles was analysed using SEM and compared to that of competitive products, i.e. natural slate stone tiles and concrete tiles with a similar visual appearance. The microstructure of the natural slate stone tiles is visualized in Fig. 8: the overview in Fig. 8 a) shows major cracks parallel to the surface. The area in frame 8.1 is presented in greater detail in Fig. 8 b) and illustrates the highly inhomogeneous microstructure of the latter: all components form

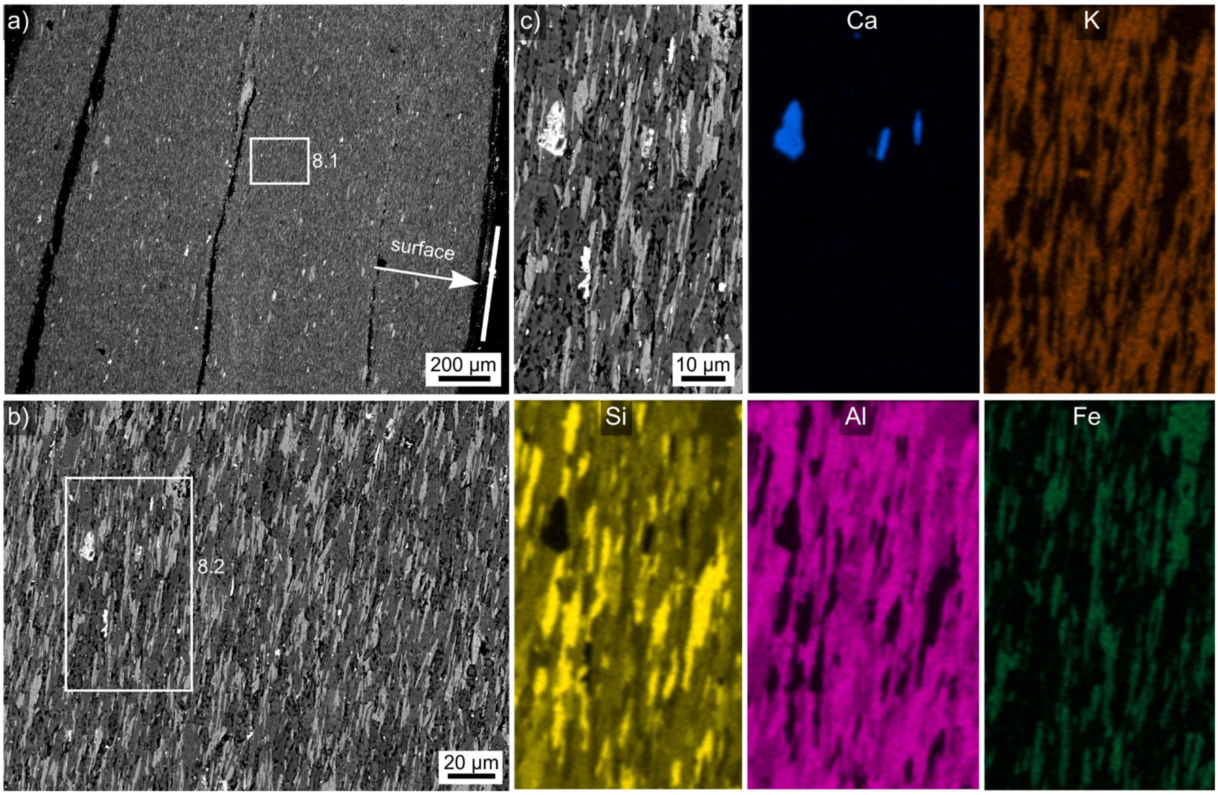

Fig. 8. SEM micrographs of a) a slate stone tile cut perpendicular to its application surface. The area in frame 8.1 is presented in greater detail in b) to visualize the anisotropic microstructure of slate. The area in frame 8.2 is presented in greater detail in c) and element maps of selected elements in this area are presented.

elongated regions parallel to the surface. Frame 8.2 marks the area presented in greater detail in Fig. 8 c) and analysed using EDXS. As slate for roofing tiles is mainly composed of quartz, mica, feldspars and chlorite [3,42], the Si-rich areas free of Al and K should represent quartz. The Ca-rich areas could represent calcite inclusions, while other phases rich in K, Fe and Al could be clay and feldspar minerals. The cracks and heterogeneous microstructure elongated parallel to the tile surface match the expectation as such stone tiles are produced by cleaving the natural stone parallel to its weak cleavage planes. Their mechanical stability parallel to the surface is hence relatively low and can allow water to enter possible cracks which degrades the tiles, especially if the water freezes.

The microstructure of the concrete tile is illustrated by Fig. 9 a) which shows the components (particles but also pores) to be generally larger than those in the natural stone tile. The black areas in the SEM micrographs are pores filled with the embedding resin which also penetrates into some concrete components, see the element map of C. The Si and Ca-enriched areas should represent CSH gel, whereas the only Ca-enriched areas should correspond to $Ca(OH)_2$ or $CaCO_3$ aggregates.

The microstructure of the AAM roofing tile in Fig. 10 a) shows large particles reaching diameters above 1 mm. EDXS element maps of the area in frame 10.1 are presented below and show particles enriched in Fe, Si, Al, and Mg, as well as spherical porosity. K is detected throughout the matrix but does not seem to penetrate the large grains, which matches the expectation as it is part of the binder/activator. Fig. 10 b) presents a segment of frame 10.1 at a higher magnification to show that the large particles (slag) appear to be partially amorphous as they contain microstructures resembling coarse (black arrows) and fine (orange arrows) dendritic growth also known from Fe-rich glass-ceramics [43]. Dendrites grow coarse at high growth velocities but become increasingly fine if the growth velocity is lowered amongst otherwise constant conditions. Assuming the dendrites in Fig. 10 are formed of the same phase, this means the coarse dendrites grew first and at high temperatures whereas the finer dendrites grew later at lower temperatures while the slag was cooled during production [44].

The area in frame 10.2 is presented in greater detail in Fig. 10 c) to highlight fine, band-like structures amongst the grains; the EDXS-map of Ca presented below shows them to be enriched in Ca. Ca enrichment in such morphologies is associated with the formation of C-A-S-H gels in AAMs [45–47], hence these structures imply a successful AAM process. These gels have been stated to be comparable to Portland cement paste and a prolonged exposure to CO_2 can lower their water permeability [48].

3.4. Life cycle assessment for the AAM roofing tiles

3.4.1. Scope of the LCA

LCA analysis was used to evaluate the environmental performance of the produced AAM roofing tiles. Its main objective was to compare their environmental impact with commercial stone or concrete tiles. The "cradle-to-gate" approach commonly used for the environmental evaluation of different building materials [49] was adopted. The LCA analysis considered the impacts related to the extraction and processing of raw materials, auxiliary materials, waste treatment, processing, and the supply of energy and water. The declared unit was specified as the production of 1 kg of material for roofing tiles. The "LCA for Experts" (formerly GaBi) software was used for modelling [50].

As Koranel® is a Fe-rich side-product from Cu production, the consequential modelling principle (i.e. system expansion) is applicable to the LCA. Hence any potential upstream environmental burden of residue materials (i.e. Cu-slag) is not transferred into the model [51]. Avoided environmental impacts of slag landfilling are, however, included. The avoided disposal of slag in a landfill is considered as an environmental credit, because it leads to the reduction in the amount of the material that needs to be landfilled and the associated negative environmental impact. Therefore, the impact of Koranel® is thus obtained by first calculating the impact related to the Cu-slag and then subtracting the impact of landfilling it (avoided process).

3.4.2. Life cycle inventory (LCI)

The production and processing of raw, secondary and ancillary materials, waste treatment and processing, as well as the production and supply of electricity and water were evaluated based on the background LCI data provided in the Sphera Managed LCA Content (formerly GaBi Professional) and Ecoinvent 3.8 databases. The main material inputs for the production of AAM roofing tile are presented in Table 2. They were cured in a laboratory-scale oven with an electricity consumption of 2 kWh per 1 kg of material. The production of stone and concrete roofing tiles was modelled based on the generic dataset in the database, which represents industrial average values.

A conventional LCA study is usually an ex-post analysis of an existing, well-defined and generally well-documented system [52]. Applying this to emerging technologies can be problematic due to the lack of real-world data. Hence the comparability of LCAs of emerging and established systems highly depends on the development stage and technological maturity of the analysed system [53]. The projected decrease in energy demand is based on analogous industrial processes and is identified as a target for validation at the pilot scale. Industrial-scale production can achieve even lower electricity

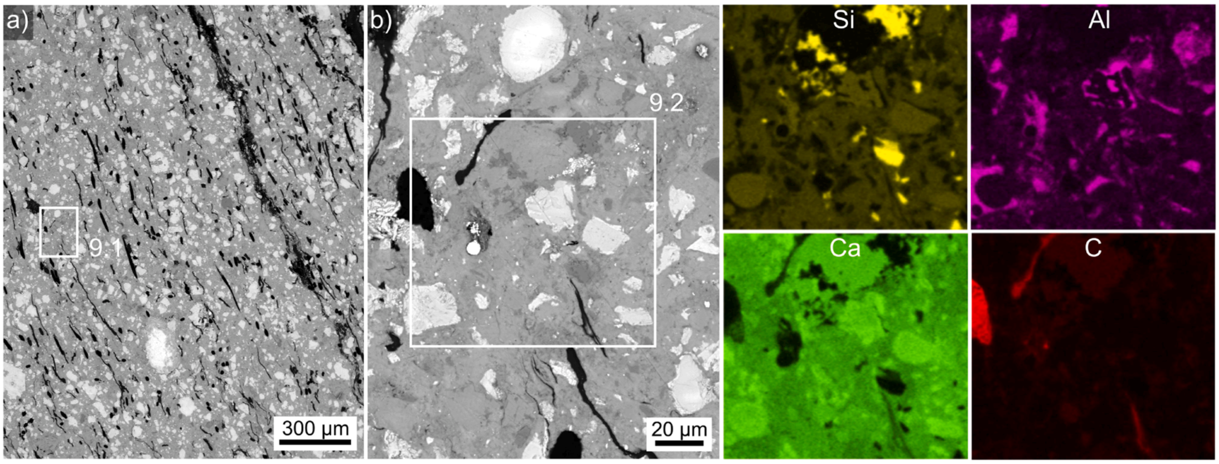

Fig. 9. SEM micrographs presenting a) an overview of the microstructure in a concrete tile and b) the area in frame 9.1 in greater detail. Selected element maps of the area in frame 9.2 are presented.

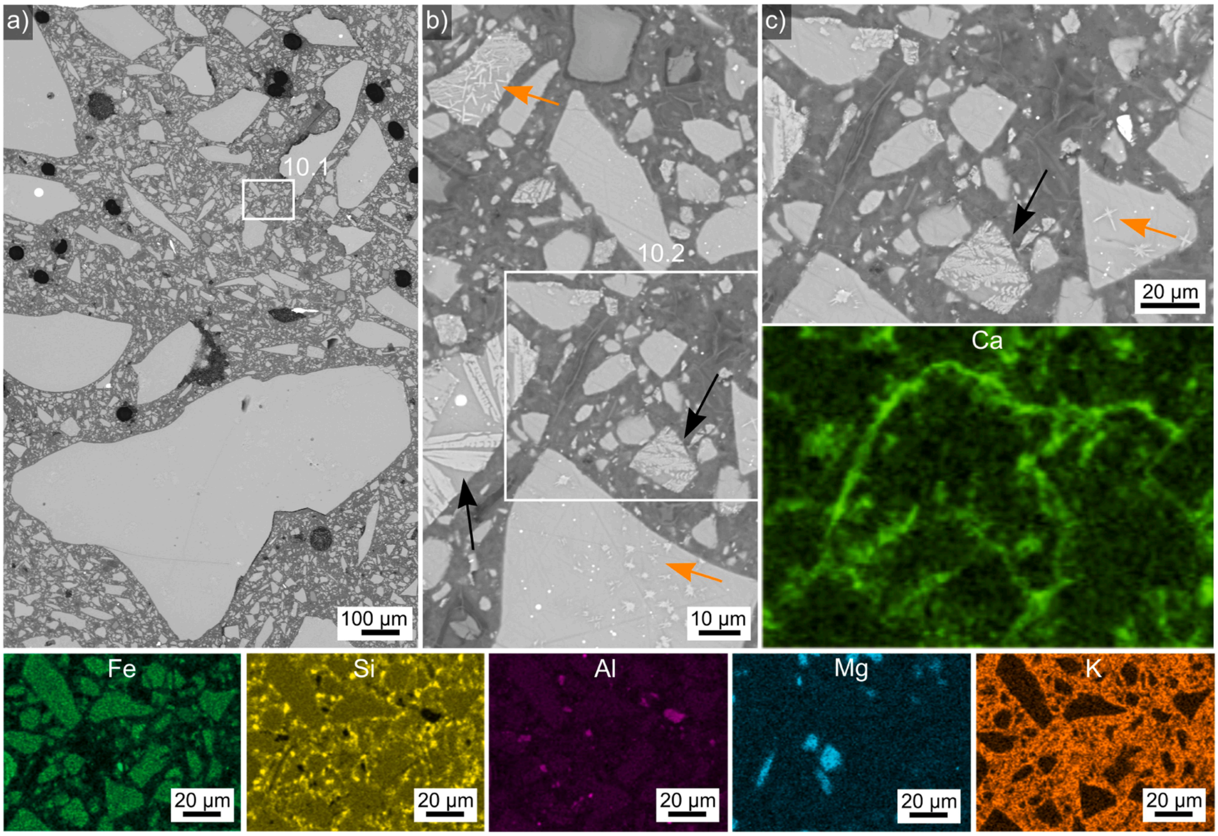

Fig. 10. a) SEM micrograph presenting an overview of the microstructure in a AAM roofing tile, selected element maps of the area in frame 10.1 are presented. b) SEM micrograph featuring the microstructure in greater detail. Substructures in some larger components are visualized by arrows. The area in frame 10.2 is presented in c) and enables to discern that these substructures are dendrites, i.e. most likely crystals in an amorphous matrix.

consumption, as indicated above: for example, the electricity consumption of industrial-scale produced concrete roofing panels can be as low as 0.002 kWh per panel [54,55]. The assumed value of 0.2 kWh per kg for curing of AAM roofing panels was therefore selected as a conservative estimate to remain on the safe side, while still reflecting the expected efficiency improvements at a larger production scale.

3.4.3. Life cycle impact assessment (LCIA)

The environmental impacts were evaluated with the CML 2001 (version Aug. 2016) LCIA method [56], which is one of the most commonly used LCIA methods in the field of LCA for AAMs [57]. LCA results are expressed via different impact categories, which cannot be directly compared amongst each other due to their different physical units unless an optional normalization step is performed. Normalization uses external information to express the results in a common scale [58]. The characterized results of each impact category are divided by a selected reference value, which brings all the results to the same scale [59]. The normalized LCA results are calculated by:

$$N = \frac{EI}{R} \tag{1}$$

where N is the normalised result, EI is the characterized impact of the impact category of the studied system, and R is the characterised impact of the impact category of the reference system. The considered impact categories and corresponding normalization factors are summarized in Table 5.

3.4.4. LCA evaluation

Fig. 11 shows the contribution analysis results for AAM roofing tiles. The electricity for the curing process is the largest contributor to the total environmental impact. 1.7KSi65 and the SRA also have a noticeable contribution to the total environmental impact, while the impact of GGBFS, M800, polypropylene fibres and electricity for milling of Koranel® is smaller. Using Koranel® has a slightly positive impact on the environmental performance (i.e., negative values in the figure) because the benefits of avoiding landfilling outweigh the impacts related to treating and processing Cu-slag.

Fig. 12 compares the normalised environmental impact of AAM, stone slab and concrete roofing tiles to that of AAM tiles produced at an

Table 5
Impact categories and normalization factors for the CML 2001 LCIA.

Indicator	Abbreviation	Unit	Normalization factor
Abiotic Depletion Potential, non-fossil resources	ADP el.	kg Sb equiv.	1.62E+08
Abiotic depletion potential, fossil resources	ADP fos.	MJ	3.51E+13
Acidification Potential	AP	kg SO_2 equiv.	1.68E+10
Eutrophication Potential	EP	kg PO_4^{3} equiv.	1.85E+10
Freshwater Aquatic Ecotoxicity Potential	FAETP	kg DCB equiv.	2.09E+11
Global Warming Potential	GWP	kg CO_2 equiv.	5.22E+12
Human Toxicity Potential (HTP, unit	HTP	kg DCB equiv.	5.00E+11
Ozone Depletion Potential	ODP	kg R11 equiv.	1.02E+07
Photochemical Ozone Creation Potential	POCP	kg Ethene equiv.	1.73E+09
Terrestrial Ecotoxicity Potential	TETP	kg DCB equiv.	1.16E+11

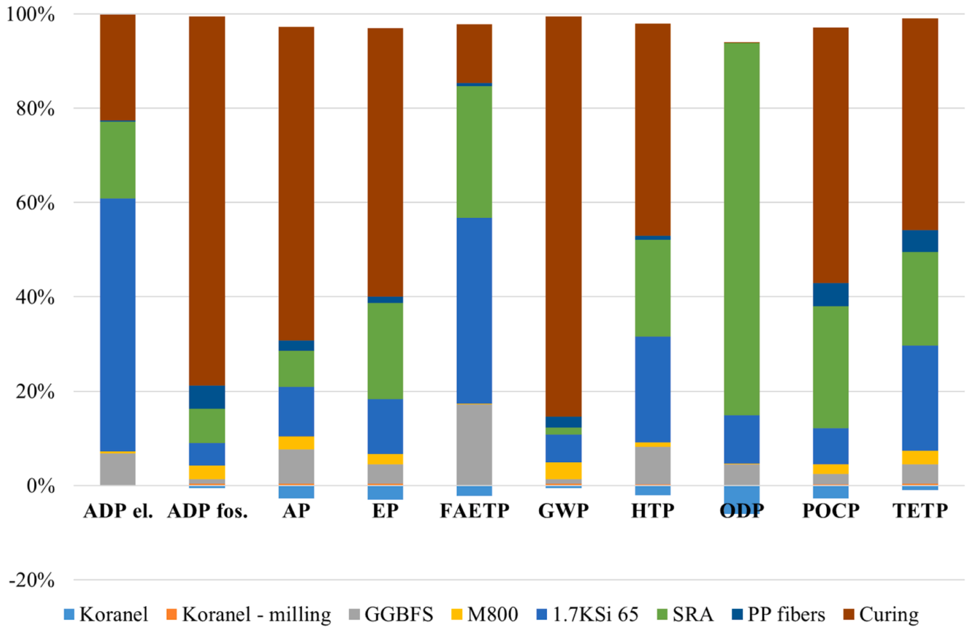

Fig. 11. Relative contributions for AAM roofing tiles (abbreviations detailed in Table 5).

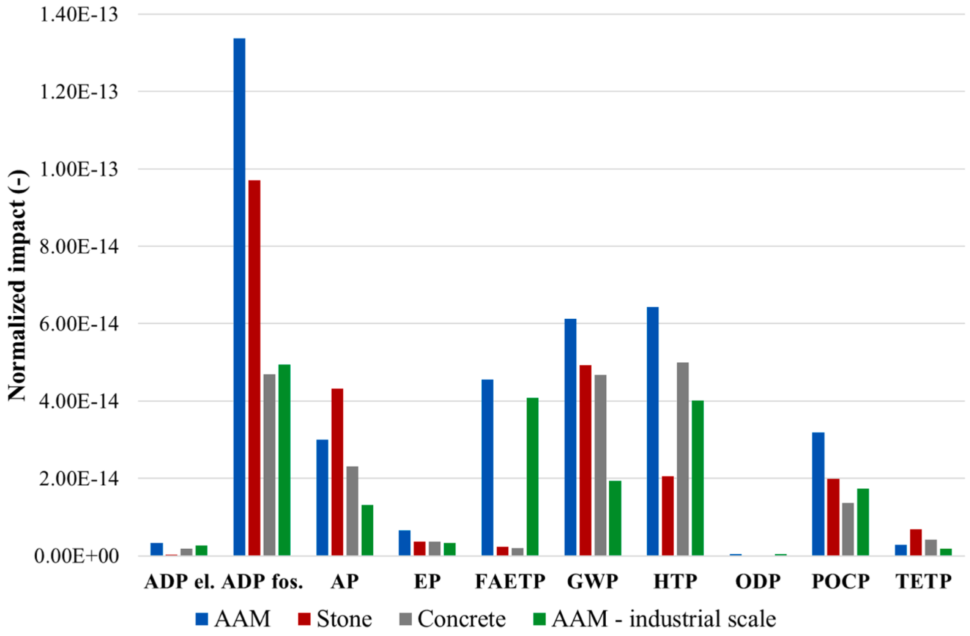

Fig. 12. Comparison of the environmental impact of AAM, stone and concrete roofing tiles. The results are for the production of 1 kg of material (abbreviations detailed in Table 5).

industrial scale (i.e., 0.2 kWh/kg for curing). It shows that the AAM roofing tile has a higher environmental impact than the commercial products. Keeping in mind that these calculations show trends and highlight major contributing factors, the respective values should not be overemphasized. The environmental impact can be notably reduced by improving the energy efficiency at the industrial-scale production, particularly with respect to the use of fossil fuels (i.e., ADP fos.) and carbon emissions (i.e., GWP).

The environmental impact of AAMs can be reduced by using by-products as activators, locally available materials, and efficient production and curing methods [27,57]. The AAM roofing tiles were produced with local industrial residue, reducing landfill volumes and transportation distances and thus improving their environmental performance.

3.5. Demonstration roof

The demonstration roof featured in Fig. 13 was installed to monitor the long-term performance of the roofing tiles over several years (four at the time of photography) of exposure to various seasons. The tiles still appear to be in good condition at the time of manuscript submission and will be further assessed in detail in the future.

In summary, this study presents a case study featuring the development of a residue-based industrial product suited to replace a natural building material of dwindling availability. In contrast to natural slate stone, the prepared product can be modified to ease the attraction of

Fig. 13. AAM roofing tiles installed on a demonstration roof. The seven tiles in the top line (arrow) were treated with an additional coating not discussed in this manuscript.

plants and mosses, should a “green roof” be desired, by manufacturing single-layer tiles composed of only the fibre layer. The main issues of mixture flow, porosity, and efflorescence were optimized by adapting the raw materials, mould material, and curing procedure. The prepared fibre layer mixture is thixotropic, allowing for easy mixing under high shear stress, while a full recovery of the high viscosity required for rolling is achieved less than one minute after the critical shear stress is removed. This is important given the comparatively short working time of approximately 45 min.

While the mechanical properties of the AAM roofing tiles fulfil the technical requirements of the relevant standards, they do fall short of comparable stone or concrete products. Further performance improvements can be achieved by e.g., optimizing the curing regime [60,61]. However, the most relevant properties, such as water impermeability and freeze-thaw resistance, are comparable, and the porosity is lower than that of slate stone. The highly anisotropic microstructure of slate stone, defining its cleavability, makes it rather sensitive to specific forces. This is not an issue in the industrial concrete or AAM roofing tiles.

4. Conclusions

The present work demonstrated the feasibility of producing slate-like roofing tiles through the alkali activation of an Fe-rich copper slag blended with GGBFS, establishing a residue-based alternative to natural slate. The double-layer design—comprising a fibre-reinforced structural layer and a visually optimized surface layer—proved essential for achieving the required mechanical performance and the targeted slate-like appearance. Optimising the mixture design, mould selection, and curing regime successfully mitigated key challenges such as excessive viscosity, porosity, and efflorescence.

The rheological investigations confirmed that the fibre layer exhibits thixotropic behaviour, enabling appropriate workability during mixing and placement, while rapidly recovering its high viscosity to allow efficient rolling and shaping. The mechanical performance of the tiles met the requirements of the relevant roofing standards, although the transverse strength remained lower than that of commercial concrete and natural slate tiles. Nevertheless, the tiles displayed excellent water impermeability and sufficient freeze–thaw resistance. MIP indicated that the pore structure of the AAM tiles is distinctive compared to that of slate and concrete tiles, with gel-pore-dominated porosity typical of AAM systems.

The microstructural analysis revealed a heterogeneous matrix composed of partially amorphous Fe-rich particles embedded in a potassium-rich alkali-activated binder. The identification of Ca-enriched areas amongst the aggregates implies the successful formation of an AAM network, consistent with the properties measured at the macroscopic scale.

The LCA results showed that the environmental performance of the laboratory-scale tiles is compromised by the high energy demand of the curing step. However, scenarios mimicking industrial-scale production—where curing can be achieved at far lower energy inputs—indicate a substantial reduction in environmental impact. The use of copper slag offers an intrinsic environmental advantage, as it avoids landfilling and reduces the consumption of primary raw materials.

Finally, the installation of a demonstration roof confirmed the practical applicability of the product and its stability under outdoor exposure over several years. With further optimization with respect to the open time, precise timing control for casting the layers and synchronizing it with vibration, such tiles could represent a promising, market-realistic, circular alternative to natural slate and concrete roofing products.

Funding

This research was funded by EIT Raw Materials project Recover+ no.16365 and by the Slovenian Research Agency (ARIS) via the research programme P2–0273.

Data availability statement

Data will be made available on request.

CRediT authorship contribution statement

Vilma Ducman: Writing – original draft, Methodology, Formal analysis, Data curation, Conceptualization. **Wolfgang Wisniewski:** Writing – review & editing, Visualization, Formal analysis, Data curation. **Afsar Muhammad:** Writing – review & editing, Methodology, Investigation, Formal analysis, Data curation. **Davor Kvočka:** Writing – review & editing, Visualization, Methodology, Formal analysis, Data curation. **Efthymios Tatsis:** Investigation, Formal analysis, Data curation. **Lubica Kriskova:** Writing – review & editing, Supervision, Methodology, Investigation, Formal analysis, Data curation. **Yiannis Pontikes:** Writing – review & editing, Validation, Supervision, Resources, Project administration, Conceptualization.

Declaration of competing interest

The authors declare that they have no known competing financial interests or personal relationships that could have appeared to influence the work reported in this paper.

Acknowledgments

This research was funded by the EIT Raw Materials project Recover+ (no. 16365) and the Slovenian Research Agency (ARIS) through the research program P2–0273. The authors would like to express their gratitude to our former colleague Theodoros Karachalios for his contributions to funding acquisition. We also extend our thanks to Catalin Dragos Tunsoiu for technical assistance and Glenn Beersaerts for conducting the rheology analyses.

References

[1] M. Lombardero, J. Garcia-Guinea, V. Cardenes, The geology of roofing slate, in: 2002: pp. 59–66.

[2] E.J.H. Charles Singer, A history of technology. Volume I. From Early Times to Fall of Ancient Empires, 1954. http://archive.org/details/B-001-001-770 (accessed November 19, 2025).

[3] V. Cárdenes, Á. Rubio-Ordoñez, V.G.R. de Argandona, Definition of roofing slate lithotypes for an international roofing slate classification, Key Eng. Mater. 848 (2020) 48–57, https://doi.org/10.4028/www.scientific.net/KEM.848.48.

[4] J. Garabito, A. Rodriguez, J.C. Garabito, V. Calderon, Durability of slate and zinc sheets in the rehabilitation of historical heritage. A case study, Constr. Build. Mater. 135 (2017) 212–224, https://doi.org/10.1016/j.conbuildmat.2016.12.224.

[5] V. Ducman, A.S. Škapin, M. Radeka, J. Ranogajec, Frost resistance of clay roofing tiles: case study, Ceram. Int. 37 (2011) 85–91, https://doi.org/10.1016/j.ceramint.2010.08.012.

[6] B. Prieto, P. Ferrer, P. Sanmartín, V. Cárdenes, B. Silva, Color characterization of roofing slates from the Iberian Peninsula for restoration purposes, J. Cult. Herit. 12 (2011) 420–430, https://doi.org/10.1016/j.culher.2011.02.001.

[7] V. Cárdenes, Á. Rubio-Ordóñez, C. Monterroso, F.J. Mateos, Guidelines for selecting roofing slate for the restoration of historical buildings and monuments: two case studies, J. Cult. Herit. 15 (2014) 203–208, https://doi.org/10.1016/j.culher.2013.02.004.

[8] F. Sitzia, C. Lisci, V. Pires, T. Alves, J. Mirão, Laboratorial simulation for assessing the performance of slates as construction materials in cold climates, Appl. Sci. 13 (2023) 2761, https://doi.org/10.3390/app13052761.

[9] W.K. Part, M. Ramli, C.B. Cheah, An overview on the influence of various factors on the properties of geopolymer concrete derived from industrial by-products, Constr. Build. Mater. 77 (2015) 370–395, https://doi.org/10.1016/j.conbuildmat.2014.12.065.

[10] Y. Qin, C. Qu, C. Ma, L. Zhou, One-part Alkali-Activated materials: State of the art and perspectives, Polymers (Basel) 14 (2022) 5046, https://doi.org/10.3390/polym14225046.

[11] M. Nawaz, A. Heitor, M. Sivakumar, Geopolymers in construction - recent developments, Constr. Build. Mater. 260 (2020) 120472, https://doi.org/10.1016/j.conbuildmat.2020.120472.

[12] J.L. Provis, Alkali-activated materials, Cem. Concr. Res. 114 (2018) 40–48, https://doi.org/10.1016/j.cemconres.2017.02.009.

[13] J. Van De Sande, A. Peys, T. Hertel, H. Rahier, Y. Pontikes, Upcycling of non-ferrous metallurgy slags: identifying the most reactive slag for inorganic polymer construction materials, Resour. Conserv. Recycl. 154 (2020) 104627, https://doi.org/10.1016/j.resconrec.2019.104627.

[14] A. Adediran, J. Yliniemi, M. Illikainen, Development of sustainable Alkali-activated mortars using Fe-rich fayalitic slag as the sole solid precursor, Front. Built Environ. 7 (2021), https://doi.org/10.3389/fbuil.2021.653466.

[15] V. Ponomar, J. Yliniemi, E. Adesanya, K. Ohenoja, M. Illikainen, An overview of the utilisation of Fe-rich residues in alkali-activated binders: mechanical properties and state of iron, J. Clean. Prod. 330 (2022) 129900, https://doi.org/10.1016/j.jclepro.2021.129900.

[16] V. Hallet, M.T. Pedersen, B. Lothenbach, F. Winnefeld, L. Eykens, N. De Belie, Y. Pontikes, The hydration of ternary blended cements with Fe-rich slag from non-ferrous metallurgy and limestone, Cem. Concr. Res. 169 (2023) 107155, https://doi.org/10.1016/j.cemconres.2023.107155.

[17] M. Giels, T. Hertel, K. Gijbels, W. Schroeyers, Y. Pontikes, High performance mortars from vitrified bauxite residue; the quest for the optimal chemistry and processing conditions, Cem. Concr. Res. 155 (2022) 106739, https://doi.org/10.1016/j.cemconres.2022.106739.

[18] G. Ascensão, M. Marchi, M. Segata, F. Faleschini, Y. Pontikes, Reaction kinetics and structural analysis of alkali activated Fe–Si–Ca rich materials, J. Clean. Prod. 246 (2020) 119065, https://doi.org/10.1016/j.jclepro.2019.119065.

[19] M. Giels, T. Hertel, P.N. Gamaletsos, V. Hallet, Y. Pontikes, Reactive precursors for inorganic polymers and blended cements from vitrified bauxite residue. A case study for Europe, Constr. Build. Mater. 491 (2025) 142459, https://doi.org/10.1016/j.conbuildmat.2025.142459.

[20] A. Frankovič, V. Ducman, L. Kriskova, E. Tatsis, P. Petrica, Y. Pontikes, The development and assessment of Alkali activated paving blocks, 2022. https://doi.org/10.18690/um.fkkt.2.2022.1.

[21] G. Beersaerts, S.S. Lucas, Y. Pontikes, in: F.P. Bos, S.S. Lucas, R.J.M. Wolfs, T.A. M. Salet (Eds.), An Fe-Rich Slag-Based Mortar for 3D Printing, Springer International Publishing, Cham, 2020, pp. 3–12, https://doi.org/10.1007/978-3-030-49916-7_1. Second RILEM Int. Conf. Concr. Digit. Fabr.

[22] P.P. Sivakumar, S. Matthys, N.D. Belie, E. Gruyaert, Reactivity assessment of modified ferro silicate slag by R3 method, Appl. Sci. 11 (2021), https://doi.org/10.3390/app11010366.

[23] P.N. Lemougna, N. Dilissen, G.M. Hernandez, F. Kingne, J. Gu, H. Rahier, Effect of sodium disilicate and metasilicate on the microstructure and mechanical properties of one-part alkali-activated copper slag/ground granulated blast furnace slag, Materials (Basel) 14 (2021), https://doi.org/10.3390/ma14195505.

[24] M. Amran, R. Fediuk, H.S. Abdelgader, G. Murali, T. Ozbakkaloglu, Y.H. Lee, Y. Y. Lee, Fiber-reinforced alkali-activated concrete: A review, J. Build. Eng. 45 (2022) 103638, https://doi.org/10.1016/j.jobe.2021.103638.

[25] M. Češnovar, K. Traven, B. Horvat, V. Ducman, The potential of ladle slag and electric arc furnace slag use in synthesizing alkali activated materials; the influence of curing on mechanical properties, Materials (Basel) 12 (2019), https://doi.org/10.3390/ma12071173.

[26] EN 491:2011 - Concrete roofing tiles and fittings for roof covering and wall cladding - test methods, ITeh Stand. 2011. https://standards.iteh.ai/catalog/standards/cen/50efc3e1-1268-440b-a4cf-6bfc2c39e7ba/en-491-2011 (accessed November 19, 2025).

[27] A. Dacić, K. Kopecskó, O. Fenyvesi, I. Merta, The obstacles to a broader application of Alkali-activated binders as a sustainable alternative—A review, Materials (Basel) 16 (2023) 3121, https://doi.org/10.3390/ma16083121.

[28] W.M. Kriven, C. Leonelli, J.L. Provis, A.R. Boccaccini, C. Attwell, V.S. Ducman, C. Ferone, S. Rossignol, T. Luukkonen, J.S.J. van Deventer, J.V. Emiliano, J. E. Lombardi, Why geopolymers and alkali-activated materials are key components of a sustainable world: A perspective contribution, J. Am. Ceram. Soc. 107 (2024) 5159–5177, https://doi.org/10.1111/jace.19828.

[29] M. Pavlin, B. Horvat, V. Ducman, Pilot production of façade panels : variability of mix design, in: 5th Int. Conf. Technol. Bus. Models Circ. Econ, 2023, pp. 25–43. University of Maribor, University Press, Faculty of Chemistry and Chemical Engineering, https://dirros.openscience.si/IzpisGradiva.php?id=17381 (accessed November 19, 2025).

[30] M. Pavlin, B. Horvat, V. Ducman, Preparation of façade panels based on alkali-activated waste mineral wool, their characterization, and durability aspects, Int. J. Appl. Ceram. Technol. 19 (2022) 1227–1234, https://doi.org/10.1111/ijac.13998.

[31] L. Kriskova, V. Ducman, M. Loncnar, A. Tesovnik, G. Žibret, D. Skentzou, C. Georgopoulos, Alkali-activated mineral residues in construction: case studies on bauxite residue and steel slag pavement tiles, Materials (Basel) 18 (2025) 257, https://doi.org/10.3390/ma18020257.

[32] G. Lamaa, A.P.C. Duarte, R.V. Silva, J. de Brito, Carbonation of alkali-activated materials: A review, Materials (Basel) 16 (2023), https://doi.org/10.3390/ma16083086.

[33] J. Hwalla, M. Al-Mazrouei, K. Al-Karbi, A. Al-Hebsi, M. Al-Ameri, F. Al-Hadrami, H. El-Hassan, Performance of Alkali-activated slag concrete masonry blocks subjected to accelerated carbonation curing, Sustainability 15 (2023), https://doi.org/10.3390/su151914291.

[34] W. Wu, J. Wang, X. Wang, L. Xu, Influence of pre-curing methods on the strength development of CO2-cured alkali-activated slag mortar with different alkali activators, Constr. Build. Mater. 500 (2025) 144120, https://doi.org/10.1016/j.conbuildmat.2025.144120.

[35] S.A. Bernal, J.L. Provis, B. Walkley, R. San Nicolas, J.D. Gehman, D.G. Brice, A. R. Kilcullen, P. Duxson, J.S.J. van Deventer, Gel nanostructure in alkali-activated binders based on slag and fly ash, and effects of accelerated carbonation, Cem. Concr. Res. 53 (2013) 127–144, https://doi.org/10.1016/j.cemconres.2013.06.007.

[36] Y. Zuo, G. Ye, Pore structure characterization of sodium hydroxide activated slag using mercury intrusion porosimetry, nitrogen adsorption, and image analysis, Materials (Basel) 11 (2018) 1035, https://doi.org/10.3390/ma11061035.

[37] S. Siddique, J.G. Jang, Mechanical properties, microstructure, and chloride content of alkali-activated fly ash paste made with sea water, Materials (Basel) 13 (2020) 1467, https://doi.org/10.3390/ma13061467.

[38] C. Grengg, G. Koraimann, N. Ukrainczyk, O. Rudic, S. Luschnig, G.J.G. Gluth, M. Radtke, M. Dietzel, F. Mittermayr, Cu- and Zn-doped alkali activated mortar – Properties and durability in (bio)chemically aggressive wastewater environments, Cem. Concr. Res. 149 (2021) 106541, https://doi.org/10.1016/j.cemconres.2021.106541.

[39] M. Huang, S. Bao, Y. Zhang, M. Li, Y. Ping, C. Lin, Durability of alkali-activated cementitious materials at freeze-thaw environment: damage and protection mechanism, Constr. Build. Mater. 488 (2025) 142102, https://doi.org/10.1016/j.conbuildmat.2025.142102.

[40] D. Liu, Y. Tu, G. Sas, L. Elfgren, Freeze-thaw damage evaluation and model creation for concrete exposed to freeze–thaw cycles at early-age, Constr. Build. Mater. 312 (2021) 125352, https://doi.org/10.1016/j.conbuildmat.2021.125352.

[41] C. Wang, Z.-L. Liu, L. Yu, Relationship between anti-frozen durability and pore structure on concrete in freeze and thaw cycle environment, in: MATEC Web Conf 238, 2018 02010, https://doi.org/10.1051/matecconf/201823802010.

[42] K. Raju, S. Ravindhar, Detailed review on natural stone materials in architecture, Mater, Today Proc 45 (2021) 6341–6347, https://doi.org/10.1016/j.matpr.2020.10.842.

[43] R. Harizanova, I. Avramova, W. Wisniewski, G. Avdeev, D. Tzankov, M. Georgieva, I. Gugov, C. Rüssel, EBSD investigation and magnetic properties of manganese ferrite crystallized in a sodium-silicate glass, CrystEngComm 20 (2018) 4268–4276, https://doi.org/10.1039/C8CE00484F.

[44] L. Gan, C. Zhang, J. Zhou, F. Shangguan, Continuous cooling crystallization kinetics of a molten blast furnace slag, J. Non-Cryst. Solids 358 (2012) 20–24, https://doi.org/10.1016/j.jnoncrysol.2011.08.008.

[45] F. Pacheco-Torgal, J.P. Castro-Gomes, S. Jalali, Adhesion characterization of tungsten mine waste geopolymeric binder. Influence of OPC concrete substrate surface treatment, Constr. Build. Mater. 22 (2008) 154–161, https://doi.org/10.1016/j.conbuildmat.2006.10.005.

[46] Z. Zhang, X. Yao, H. Zhu, Potential application of geopolymers as protection coatings for marine concrete: II. Microstructure and anticorrosion mechanism, Appl. Clay Sci. 49 (2010) 7–12, https://doi.org/10.1016/j.clay.2010.04.024.

[47] R. San Nicolas, J.L. Provis, The interfacial Transition zone in Alkali-activated slag mortars, Front. Mater. 2 (2015), https://doi.org/10.3389/fmats.2015.00070.

[48] Y. Zhang, Y. He, X. Cui, L. Liu, Enhancing freeze–Thaw resistance of Alkali-activated slag by Metakaolin, ACS Omega 8 (2023) 20869–20880, https://doi.org/10.1021/acsomega.3c01600.

[49] V.G. Larsen, N. Tollin, P.A. Sattrup, M. Birkved, T. Holmboe, What are the challenges in assessing circular economy for the built environment? *A literature review on integrating LCA, LCC and S-LCA in life cycle sustainability assessment, LCSA*, J. Build. Eng 50 (2022) 104203, https://doi.org/10.1016/j.jobe.2022.104203.

[50] D.A. Lopes Silva, A.O. Nunes, C.M. Piekarski, V.A. da Silva Moris, L.S.M. de Souza, T.O. Rodrigues, Why using different Life Cycle Assessment software tools can generate different results for the same product system? A cause–effect analysis of the problem, Sustain. Prod. Consum. 20 (2019) 304–315, https://doi.org/10.1016/j.spc.2019.07.005.

[51] B. Weidema, Avoiding Co-product allocation in life-cycle assessment, J. Ind. Ecol. 4 (2000) 11–33, https://doi.org/10.1162/108819800300106366.

[52] S. Cucurachi, C. van der Giesen, J. Guinée, Ex-ante LCA of Emerging Technologies, Procedia CIRP 69 (2018) 463–468, https://doi.org/10.1016/j.procir.2017.11.005.

[53] S. Weyand, K. Kawajiri, C. Mortan, L. Schebek, Scheme for generating upscaling scenarios of emerging functional materials based energy technologies in prospective LCA (UpFunMatLCA), J. Ind. Ecol. 27 (2023) 676–692, https://doi.org/10.1111/jiec.13394.

[54] D.M. de Souza, M. Lafontaine, F. Charron-Doucet, X. Bengoa, B. Chappert, F. Duarte, L. Lima, Comparative Life cycle Assessment of ceramic versus concrete roof tiles in the Brazilian context, J. Clean. Prod. 89 (2015) 165–173, https://doi.org/10.1016/j.jclepro.2014.11.029.

[55] Dataset Search | ecoQuery, (2025). https://ecoquery.ecoinvent.org/3.10/cutoff/search (accessed November 19, 2025).

[56] J.B. Guinee, Handbook on life cycle assessment operational guide to the ISO standards, Int. J. Life Cycle Assess. 7 (2002) 311–313, https://doi.org/10.1007/BF02978897.

[57] M. Nikravan, R. Firdous, D. Stephan, Life cycle assessment of alkali-activated materials: a systematic literature review, Low-Carbon Mater. Green Constr. 1 (2023) 13, https://doi.org/10.1007/s44242-023-00014-6.

[58] A. Hélias, R. Servien, Normalization in LCA: how to ensure consistency? Int. J. Life Cycle Assess. 26 (2021) 1117–1122, https://doi.org/10.1007/s11367-021-01897-y.

[59] V. Aymard, V. Botta-Genoulaz, Normalisation in life-cycle assessment: consequences of new European factors on decision-making, Supply Chain Forum Int. J. 18 (2017) 76–83, https://doi.org/10.1080/16258312.2017.1333385.

[60] M. Češnovar, K. Traven, B. Horvat, V. Ducman, The potential of ladle slag and electric arc furnace slag use in synthesizing alkali activated materials; the influence of curing on mechanical properties, Materials (Basel) 12 (2019) 1173, https://doi.org/10.3390/ma12071173.

[61] R. Murillo Alarcón, T. Hertel, E. François, H. Rahier, Y. Pontikes, Forming zeolites and calcium silicate hydrates in Fe-rich, slag-based, porous inorganic polymers, Cem. Concr. Res. 153 (2022) 106655, https://doi.org/10.1016/j.cemconres.2021.106655.